
IMPACTS OF RUDDER PROFILES ON SHIP MANOEUVRABILITY

Jialun Liu, Delft University of Technology, Delft, The Netherlands.

Frans Quadflieg, MARIN (Maritime Research Institute Netherlands), Wageningen, The Netherlands.

Robert Hekkenberg, Delft University of Technology, Delft, The Netherlands.

THE PERFORMANCE OF A SHIP'S RUDDER LARGELY DETERMINES ITS MANOEUVRABILITY, WHICH INCLUDES TURNING ABILITY, INITIAL TURNING ABILITY, YAW-CHECKING ABILITY AND COURSE-KEEPING ABILITY. HOWEVER, EXISTING EMPIRICAL FORMULAS FOR RUDDER FORCES DO NOT CONCERN THE RUDDER PROFILE. THIS PAPER DISCUSSES THE IMPACTS OF VARIOUS RUDDER PROFILES ON SHIP MANOEUVRABILITY. INSTEAD OF EMPIRICAL FORMULAS FOR RUDDER CHARACTERISTICS, COMPUTATIONAL FLUID DYNAMIC METHODS (CFD) ARE APPLIED TO OBTAIN LIFT AND DRAG COEFFICIENTS OF FIVE PROFILES. THEN, THE NORMAL FORCE COEFFICIENT OF EACH PROFILE IS CALCULATED AND CORRECTED FOR THE ASPECT RATIO. COMMERCIAL PACKAGES POINTWISE AND ANSYS ICEM GENERATE THE UNSTRUCTURED AND STRUCTURED MESH, RESPECTIVELY. ANSYS FLUENT SOLVES THE NAVIER-STOKES EQUATIONS. 2D STEADY-STATE VISCOUS SIMULATIONS OF RUDDERS IN INCOMPRESSIBLE WATER ARE CARRIED OUT WITH THE K-W SST TURBULENCE MODEL. TO TEST THE IMPACTS ON MANOEUVRABILITY, A MANOEUVRING MODEL IS BUILT IN PYTHON FOR THE KVLCC2 TANKER IN DEEP WATER. TURNING CIRCLE MANOEUVRES AND ZIGZAG MANOEUVRES ARE PERFORMED TO COMPARE THE MANOEUVRING PARAMETERS. THIS PAPER CONCLUDES WITH INSIGHTS INTO THE IMPACTS OF RUDDER PROFILES ON SHIP MANOEUVRABILITY.

INTRODUCTION

Ship manoeuvrability determines the ship's responses to navigation orders, affecting navigation safety. To obtain sufficient manoeuvrability, designers need to predict the impacts of each ship component, i.e. the hull, the propeller, and the rudder, and their interactions. Among these components, the rudder plays an important role on ship manoeuvrability including turning ability, initial turning ability, yaw-checking ability, and course-keeping ability.

The side force Y_R (normal to the ship's centreline) is the main contribution of rudder forces on ship manoeuvring. This side force is mainly affected by the rudder area, inflow velocity, and rudder hydrodynamic coefficients. The rudder inflow velocity is related to ship sailing conditions, such as the ship speed and propeller parameters. The rudder area is limited by the ship draught. These two factors are commonly fixed for specified ship particulars. Thus, rudder hydrodynamic performance is the key impact factor to improve the rudder performance in manoeuvring.

Various rudder profiles have different hydrodynamic performances [8]. In common manoeuvring models [9], rudder forces are estimated by empirical estimates of the rudder's normal force [1]. However, these methods do not specify the rudder profile. In fact, a good

choice of the rudder profile can increase the rudder's contribution to manoeuvring and reduce the rudder induced resistance.

This paper applies CFD simulations for various rudder profiles to calculate the rudder normal force coefficient. New regression formulas are proposed for five profiles with an aspect ratio correction. A manoeuvring model is built on the KVLCC2 tanker to discuss the effects of rudder profiles on ship manoeuvring performance in turning manoeuvres and zigzag manoeuvres.

BACKGROUND

RUDDER PROFILES

Various rudder profiles are selected according to the requirements of hydrodynamic characteristics, erosion performance, and steering gear capacity. The most general choice is the NACA series as they are effective (high lift) and economical (low drag) [3]. Other profiles are HSVA series, IFS series, Schilling rudders, and flat plate rudders. This paper focuses on the NACA series. Five profiles are tested, i.e. NACA 0012, NACA 0015, NACA 0018, NACA 0021, and NACA 0024, as shown in Figure 1.

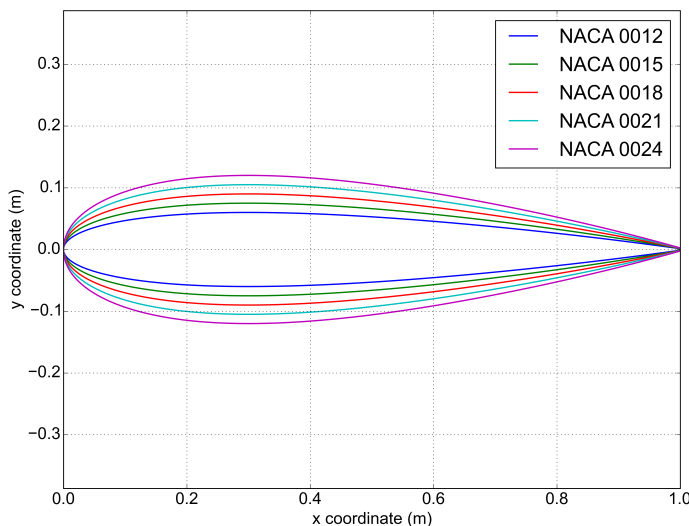


FIGURE 1 - APPLIED NACA SERIES PROFILES

EMPIRICAL METHODS

The rudder normal force F_N , based on which rudder forces in manoeuvring are calculated, is expressed as Equation 1,

$$F_N = 0.5\rho A_R U_R^2 C_N,$$

EQUATION 1

where ρ is the water density, A_R is lateral movable rudder area, U_R is the rudder inflow velocity, and C_N is the rudder normal force coefficient. The rudder axial force is commonly neglected in many simulation programs, although this may not be correct.

In general, the rudder normal force coefficient C_N is estimated by empirical methods. Fujii's formula [1] is widely used to determine the rudder normal coefficient as,

$$C_N = \frac{6.13 \cdot \Lambda}{\Lambda + 2.25} \sin \alpha_R,$$

EQUATION 2

where Λ is the rudder aspect ratio, α_R is the effective angle of attack. As this formula does not consider the profile of the rudder, it cannot be used to compare the impacts of different rudder profiles on the normal force. Therefore, Computational Fluid Methods (CFD) are used to calculate the rudder normal force coefficient.

CFD METHODS

As a primary study, this paper applies Reynolds-Averaged Navies-Stokes (RANS) simulations for various rudder profiles to assess their influence on manoeuvrability.

MESH GENERATION

A mesh presents the physical domain in a discrete form on which the governing equations can be resolved numerically. A high-quality mesh is essential to achieve converged and accurate results. Structured mesh and unstructured mesh are the two main mesh categories. Comparing these two types of mesh, a structured mesh is more efficient and accurate while an unstructured mesh is more convergence-friendly for complex geometries. In order to examine the solver usability and mesh quality, structured and unstructured meshes are both generated on a classic validation profile, i.e. NACA 0012.

Figure 2 shows the structured C-type mesh generated by ANSYS ICEM. A grid independence study was carried out first to refine the boundary layer mesh, the chord-wise size of cells around the profile, and the domain size. The profile is covered with 50 layers of structured cells to capture the viscous effects. The layer-wise and chord-wise size of the first-layer cell is 4.46E-6 c and 1.78E-03 c respectively, where c is the unit chord length. This set of boundary layers ensures an y^+ of 1 for the $k-w$ SST turbulence solver. The domain has a radius of 30 c round the profile and a length of 60 c after the profile to minimize the influences of the far-field boundary.

Figure 3 presents the unstructured mesh generated by POINTWISE. The unstructured mesh has the same boundary cells as the structured one for turbulence modelling. The domain is simplified to a rectangle of 90 c by 60 c. The main difference between the two meshes in Figure 2 and Figure 3 is the shape of the cells (quad or triangular) from the boundary layer to the far-field boundary. This distinction affects the accuracy and speed of convergence of the RANS simulations.

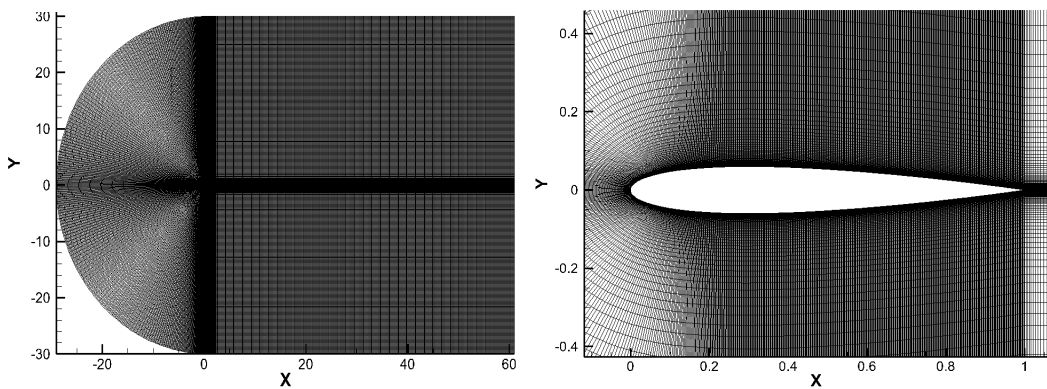


FIGURE 2 - STRUCTURED MESH GENERATED BY ANSYS ICEM AROUND NACA 0012 (LEFT) AND DETAIL CLOSE TO THE PROFILE (RIGHT)

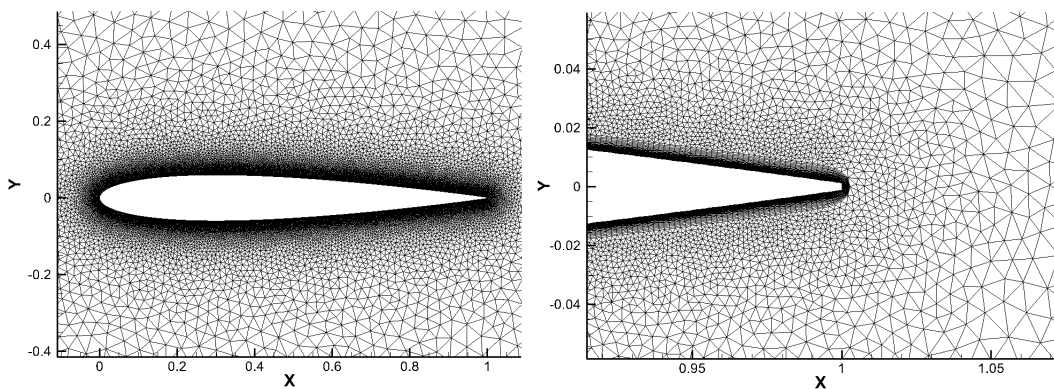


FIGURE 3 - UNSTRUCTURED MESH GENERATED BY POINTWISE AROUND NACA 0012 (LEFT) AND DETAIL CLOSE TO THE BOUNDARY LAYERS (RIGHT)

NUMERICAL METHODS

Instead of solving the continuous governing partial equations, the Navier-Stokes equations are actually solved in the discrete form of a domain, i.e. the mesh, in a numerical solver. On the other hand, turbulence models are associated with the solver to construct turbulent effects. This paper applies the ANSYS Fluent finite-volume pressure-based incompressible solver with $k-\omega$ turbulence model. To obtain sufficient accuracy, second-order upwind methods are applied for pressure, momentum, turbulent kinetic energy, and specific dissipation rate discretization. Residuals are expected to drop by at least four orders.

MODEL VALIDATION

To assess the usability of the mesh, both structured mesh and unstructured mesh are evaluated with the same solver. Initial studies show that an increase of Reynolds number decreases its impacts on lift and drag coefficients. After a Reynolds number of 6 million, the impacts can be neglected [4]. Results from FLUENT are compared to three 2D NACA 0012 aerofoil validation cases by CFL3D (NASA Larch, USA), FUN3D (NASA Larch, USA), and NTS (NTS, Russia) [5]. The relative difference between the models is calculated at each attack angle of α through Equation 3 and presented in percentage,

$$\Delta C_\alpha = \frac{C_{\alpha CFD}}{C_{\alpha Exp}} - 1.$$

EQUATION 3

Table 1 and Table 2 compare the accuracy of the structured mesh and unstructured mesh for lift and drag coefficients. Both meshes show a consistent underestimation of lift and an overestimation of drag. The underestimation is mainly caused by the numerical diffusion. The overestimation is primarily introduced by the assumption of a fully turbulent flow along the profile. In fact, the flow along the profile always starts as a laminar flow and transforms to a turbulent flow. The relative differences of lift holds steady around -1.5% as the angle of attack increases while the relative differences of drag increase. We, therefore, conclude that both meshes can provide a high accuracy of lift coefficients. The unstructured mesh is worse in drag prediction than the structured mesh. Considering the contribution of drag to the rudder-induced side force, the accuracy of drag is less important than that of lift for manoeuvring simulations.

TABLE 1 - RELATIVE DIFFERENCES OF NACA 0012 WITH STRUCTURED MESH AGAINST BENCHMARK CFD DATA IN PERCENTAGE

| | $\Delta Cd0$ (%) | $\Delta Cl5$ (%) | $\Delta Cd5$ (%) | $\Delta Cl15$ (%) | $\Delta Cd15$ (%) |
|--------------|------------------|------------------|------------------|-------------------|-------------------|
| CFL3D | 0.37 | -1.45 | 4.85 | -1.41 | 2.57 |
| FUN3D | 0.50 | -2.01 | 3.43 | -1.68 | 0.04 |
| NTS | 0.37 | -1.33 | 3.60 | -1.62 | 4.07 |

TABLE 2 - RELATIVE DIFFERENCES OF NACA 0012 WITH UNSTRUCTURED MESH AGAINST BENCHMARK CFD DATA IN PERCENTAGE

| | $\Delta Cd0$ (%) | $\Delta Cl5$ (%) | $\Delta Cd5$ (%) | $\Delta Cl15$ (%) | $\Delta Cd15$ (%) |
|--------------|------------------|------------------|------------------|-------------------|-------------------|
| CFL3D | 2.47 | -1.45 | 13.83 | -1.90 | 18.34 |
| FUN3D | 2.60 | -2.01 | 12.29 | -2.17 | 15.43 |
| NTS | 2.47 | -1.33 | 12.47 | -2.11 | 20.07 |

Comparing with experimental results [4], Figure 4 illustrates further validation of the usability of the solver with unstructured mesh. The Fluent results of lift are well matched to the experimental results, but the results of drag are gradually overestimated. The good coincidence of RANS results and experimental results validates the mesh and solver.

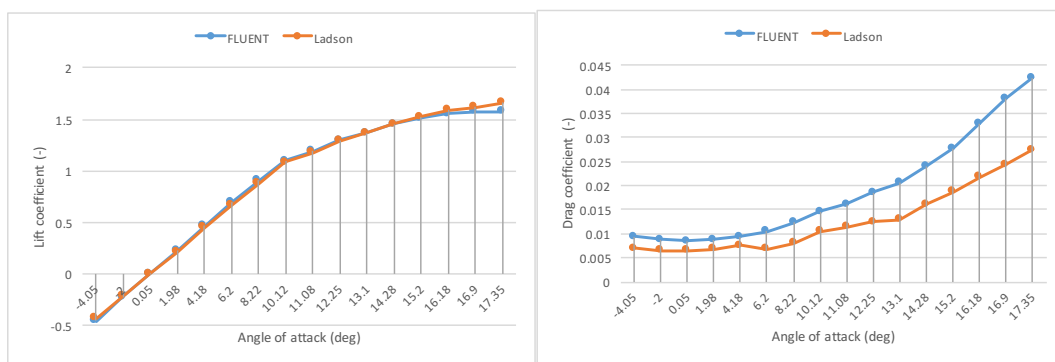


FIGURE 4 – COMPARISON OF FLUENT RESULTS OF UNSTRUCTURED MESH (PRESENT STUDY) TO EXPERIMENTAL RESULTS [4] IN LIFT (LEFT) AND DRAG (RIGHT) COEFFICIENTS

With the validated solver, the unstructured mesh is applied for the following study. First of all, lift is the main component of the rudder normal force used in manoeuvring. A good estimation of various rudders' lift is actually the goal of the applied RANS simulations. Second, during validation tests, an unstructured mesh is more convergence-friendly at large angles of attack. Last, the unstructured mesh is more convenient to generate, making it easier to be applied as a module of the whole manoeuvring simulation. Therefore, in this paper, unstructured meshes are applied for RANS simulations of various rudder profiles.

MANOEUVRING MODELLING

This paper presents manoeuvring simulations of turning manoeuvres and zigzag manoeuvres based on a MMG model [2] [9]. The MMG model expresses ship hydrodynamic forces as hull forces, propeller forces, and rudder forces, which makes it possible to analyse each component's effects on manoeuvrability. In the following section, the reference ship and coordinate system are introduced. Second, equations of motion for a single propeller and single rudder ship are presented. After that, methods applied for hull forces, propeller forces, and rudder forces are described respectively.

THE REFERENCE SHIP

The KVLCC2 tanker is selected as the reference ship. Table 3 presents the main particulars of the full-scale and model-scale ship. Free running tests of the model-scale ship were carried out by MARIN [7].

TABLE 3 - SHIP PARTICULARS OF A KVLCC2 TANKER

| Model | Full-scale | Model-scale (1:45.7) |
|--|------------|----------------------|
| Main particulars | | |
| L_{PP} (m) | 320 | 7 |
| B_{wl} (m) | 58 | 1.1688 |
| D (m) | 30 | 0.6563 |
| T (m) | 20.8 | 0.455 |
| $Disp.$ (m ³) | 312622 | 3.2724 |
| C_b (-) | 0.8098 | 0.8098 |
| C_m (-) | 0.998 | 0.998 |
| xG (m) | 11.1 | 0.244 |
| Propeller | | |
| D (m) | 9.86 | 0.204 |
| P/D (0.7R) (-) | 0.721 | 0.808 |
| A_e/A_o (-) | 0.431 | 0.448 |
| Hub ratio | 0.155 | 0.165 |
| Rudder (without the horn part) | | |
| <i>Moveable lateral area S</i> (m ²) | 115.04 | 0.0539 |
| Geometric aspect ratio | 1.827 | 1.827 |
| Turn rate (deg/s) | 2.34 | 15.8 |
| Service speed (deep water) | | |
| U (m/s, full scale: kn) | 15.5 | 1.179 |

CORRDINATE SYSTEMS

Figure 5 illustrates the applied earth-fixed coordinate system $o_0-x_0y_0z_0$ and body-fixed coordinate system $o\text{-}xyz$. The x_0y_0 surface of the earth-fixed coordinate system presents the still water surface, where the reference ship sails, and the z_0 axis points vertically downwards. The moving body-fixed coordinate system is right-handed, horizontal with x positive forward on midship (o), y positive starboard of centreline, and z positive down from waterline. The Centre of gravity of the ship G is located at $(x_G, 0, (KG-T))$ in $o\text{-}xyz$. (x_{OG}, y_{OG}) represents the ship location in $o_0\text{-}x_0y_0z_0$. The z -axis is further not considered, as in this stage, only a 3-dof simulation model is used.

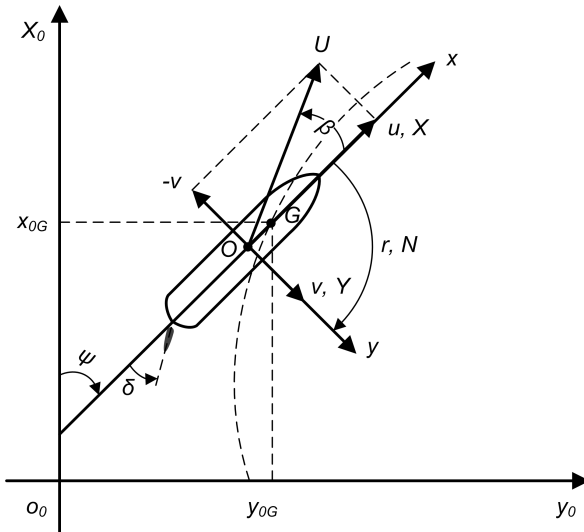


FIGURE 5 – COORDINATE SYSTEMS

In this paper, if not specified, parameters are defined on midship, subscript G is used to denote parameters defined at centre of gravity, u and v denote velocity components in x -axis and y -axis on midship, the resultant velocity is $U = \sqrt{u^2 + v^2}$, r is the yaw rate, drift angle β is the angle between u and U as $\beta = \tan^{-1}(-v/u)$, heading angle ψ is the angle between x_0 and x axes, and δ is the rudder angle.

The superscript prime indicates non-dimensionalized values. Velocity (u, v, r), force (X, Y), moment (N), mass (m), and moment of inertia (I_{zG}, J_z) are non-dimensionalized as Equation 4,

$$\left. \begin{aligned} u', v' &= \frac{u}{U}, \frac{v}{U} \\ r' &= \frac{rL_{pp}}{U} \\ X', Y' &= \frac{X}{0.5\rho L_{pp} T U^2}, \frac{Y}{0.5\rho L_{pp} T U^2} \\ N' &= \frac{N}{0.5\rho L_{pp}^2 T U^2} \\ m' &= \frac{m}{0.5\rho L_{pp}^2 T} \\ I'_{zG}, J'_z &= \frac{I_{zG}}{0.5\rho L_{pp}^4 T}, \frac{J_z}{0.5\rho L_{pp}^4 T} \end{aligned} \right\}$$

EQUATION 4

where L_{pp} is the ship length between perpendiculars, and T is the ship draught.

EQUATIONS OF MOTION

Equations of motions presented in this article are expressed as surge, sway, and yaw. First, ship motions are described as Equation 5,

$$\left. \begin{aligned} m(\dot{u}_G - v_G r) &= F_x \\ m(\dot{v}_G + u_G r) &= F_y \\ I_{zG}\dot{r} &= M_z \end{aligned} \right\},$$

EQUATION 5

where velocities at centre of gravity $u_G = u$ and $v_G = v + x_G r$, F_x , F_y , and M_z represent external forces and moments acting at centre of gravity in the direction of x-axis, y-axis, and around z-axis, m is the ship's mass, \dot{u}_G , \dot{v}_G , and \dot{v}_G are derivatives of the quantities, and I_{zG} is the moment of inertia of the ship around the centre of gravity. Considering the added mass m_x , m_y , and added moment of inertia J_z , the equations on midship to solve are presented as

$$\left. \begin{aligned} (m + m_x)\dot{u} - (m + m_y)v - x_G m r^2 &= X_H + X_P + X_R \\ (m + m_y)\dot{v} + (m + m_x)u + x_G m \dot{r} &= Y_H + Y_R \\ (I_{zG} + x_G^2 m + J_z)\dot{r} + x_G m(\dot{v} + u r) &= N_H + N_R \end{aligned} \right\},$$

EQUATION 6

where X , Y , and N are forces and moments on midship, subscript H , P , and R indicate hull, propeller, and rudder, respectively. Unknown variables u , v , and r can be determined through Equation 6 and applied to integrate trajectories of the ship's centre of gravity in the earth-fixed coordinate system through

$$\left. \begin{aligned} \dot{x}_{0G} &= u \cos \psi - (v + x_G r) \sin \psi \\ \dot{y}_{0G} &= u \sin \psi + (v + x_G r) \cos \psi \\ \dot{\psi} &= r \end{aligned} \right\}.$$

EQUATION 7

HULL FORCES

According to Yasukawa & Yoshimura (2014) [9], forces acting on the ship's hull are estimated by polynomials of the non-dimensionalized lateral velocity v' and the yaw rate r' as Equation 8,

$$\left. \begin{aligned} X_H &= 0.5\rho L_{pp} T U^2 (X'_0 + X'_{vv} v'^2 + X'_{vr} v' r' + X'_{rr} r'^2 + X'_{vvvv} v'^4) \\ Y_H &= 0.5\rho L_{pp} T U^2 (Y'_v v' + Y'_R r' + Y'_{vvv} v'^3 + Y'_{vvr} v'^2 r' + Y'_{vrr} v' r'^2 + Y'_{rrr} r'^3) \\ N_H &= 0.5\rho L_{pp}^2 T U^2 (N'_v v' + N'_R r' + N'_{vv} v'^3 + N'_{vvr} v'^2 r' + N'_{vrr} v' r'^2 + N'_{rrr} r'^3) \end{aligned} \right\},$$

EQUATION 8

where R'_0 is the ship's resistance coefficient in straight moving, Y'_v , N'_v , Y'_R , N'_R are linear hydrodynamic derivatives with respect to lateral velocity and yaw rate, respectively, X'_{vv} , X'_{vr} , X'_{rr} , X'_{vvvv} , Y'_v , Y'_{vvv} , Y'_{vvr} , Y'_{vrr} , N'_v , N'_{vvv} , N'_{vvr} , N'_{vrr} , and N'_{rrr} are hydrodynamic coefficients from model tests, which are referred to Yasukawa & Yoshimura (2014) [9].

PROPELLER FORCES

Propeller surge force X_P can be expressed as Equation 9,

$$\left. \begin{aligned} X_P &= (1 - t_P)T \\ T &= \rho n_P^2 D_P^4 K_T \\ K_T &= k_2 J_P^2 + k_1 J_P + k_0 \\ J_P &= \frac{u(1-\omega_P)}{n_P D_P} \end{aligned} \right\},$$

EQUATION 9

where t_P is the propeller thrust deduction factor, T is the propeller thrust, n_P is the propeller rate of revolution, D_P is the propeller diameter, K_T is the propeller open water thrust coefficient, J_P is the propeller advance ratio, and ω_P is the wake factor at the propeller position in manoeuvring.

RUDDER FORCES

Based on the rudder normal force F_N , the rudder forces X_R , Y_R , and N_R are expressed as,

$$\left. \begin{aligned} X_R &= -(1 - t_R)F_N \sin \delta \\ Y_R &= -(1 + a_H)F_N \cos \delta \\ N_R &= -(x_R + a_H x_H)F_N \cos \delta \end{aligned} \right\},$$

EQUATION 10

where t_R is the steering resistance deduction factor, a_H is rudder force increase factor, x_G is the longitudinal position of the rudder, and x_H is the longitudinal position of the additional lateral force.

RESULTS AND DISCUSSIONS

REFERENCE RUDDER HYDRODYNAMIC CHARACTERISTICS

Five NACA profiles are tested with 2D CFD simulations for lift and drag coefficients. Thus, the aspect ratio is considered as infinite. Instead of an empirical estimation, the normal force coefficient is calculated as

$$C_N = C_L \cos \alpha_R + C_D \sin \alpha_R.$$

EQUATION 11

As shown in Figure 6, lift coefficient decreases with the increase of profile thickness. In Figure 7, before the stall angle, thinner profiles have slightly smaller drag coefficients than the thicker ones. However, due to stronger flow separation, thinner profiles induce more drag after the stall angle. Figure 8 illustrates that thinner profiles have higher lift to drag ratios, i.e. more efficient, than thicker ones within small attack angles. After the stall angle, thinner profiles' lift to drag ratio drops sharply. For large attack angles, various profiles have basically the same performance. With higher lift and lower drag, thinner profiles have higher normal force coefficients than thicker ones, as shown in Figure 9.

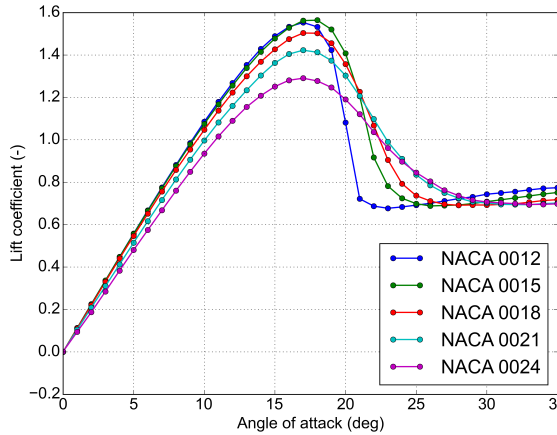


FIGURE 6 - LIFT COEFFICIENTS

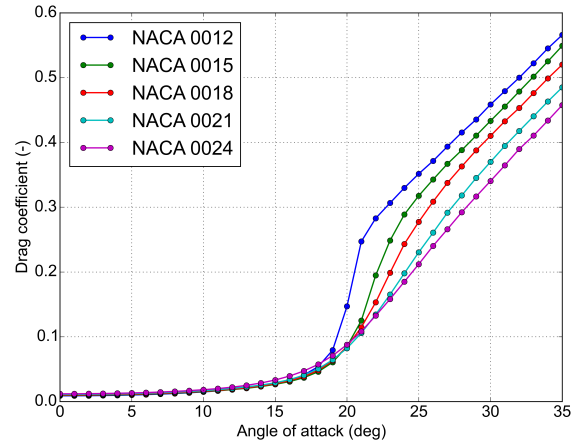


FIGURE 7 - DRAG COEFFICIENTS

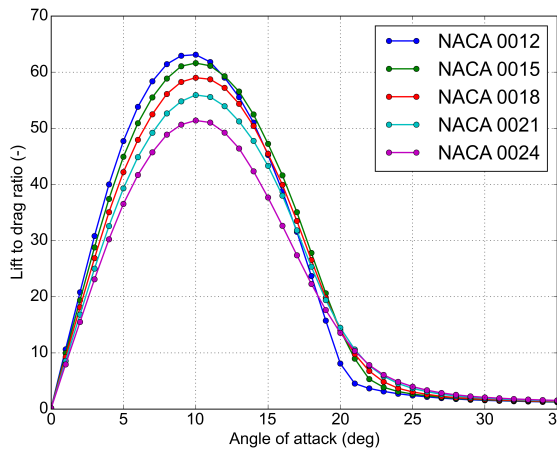


FIGURE 8 - LIFT TO DRAG RATIOS

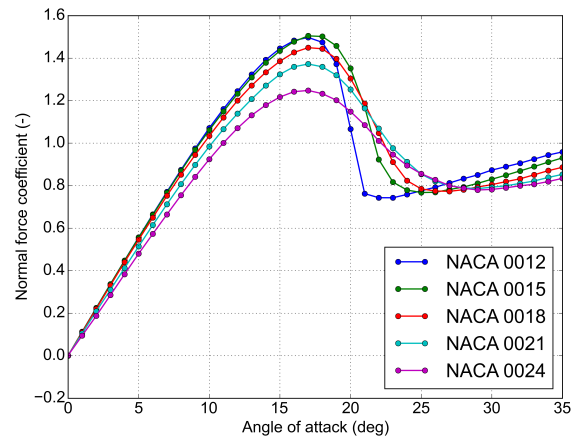


FIGURE 9 - NORMAL FORCE COEFFICIENTS

The presented results in the Figure 6 through Figure 9 are hydrodynamic coefficients of rudders with infinite aspect ratio in open water. To apply these results in manoeuvring simulations, a correction of the aspect ratio and the propeller effects is needed. The normal force coefficient of rudders with specified aspect ratio can be determined based on the coefficient of rudders with infinite aspect ratio as

$$\frac{C_{N(\Lambda=\infty)}}{C_N} = 1 + \frac{k_\Lambda}{\Lambda},$$

EQUATION 12

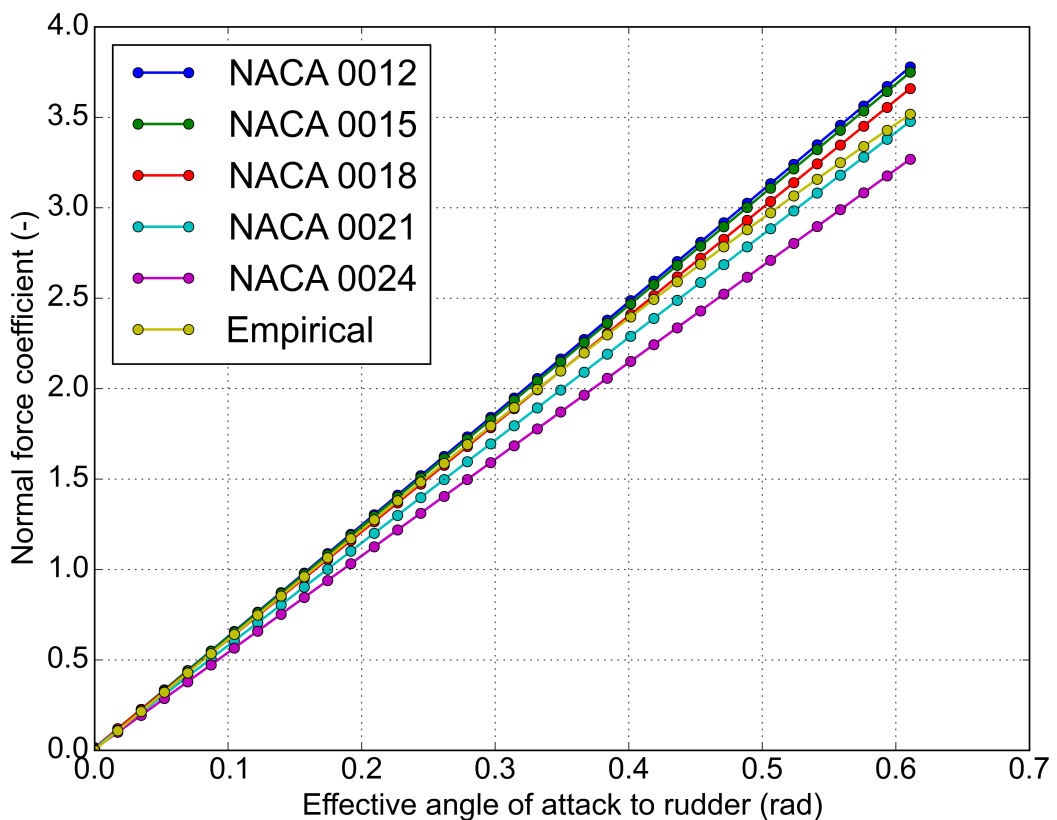
where Λ is the rudder aspect ratio, k_Λ is the aspect ratio impact factor. Compared Equation 2 with Equation 12, the $C_{N(\Lambda=\infty)}$ of Fujii's method is $6.13 \sin \alpha$ and k_Λ is 2.25. In this paper, $C_{N(\Lambda=\infty)}$ is predicted using CFD and k_Λ is set as the same as Fujii's formula.

For rudders in propeller inflow, the stall angle shifts from around 15° to about 40° [6] [8]. Before the stall angle the lift and drag curves increase at a relatively constant gradient, which is shown in Figure 6 and Figure 7. Therefore, the lift and drag coefficients of rudders in propeller flow can be predicted with the data points of rudders in open water before the stall angle. Then, the rudder normal force coefficient can be calculated as Equation 11. In this paper, the data points are selected from 0° to 10°. A least squares polynomial fit is applied to get the regression formulas for each rudder profile, as presented in Table 4. The predicted

normal force coefficients are compared with the empirical formula in Figure 10, which shows that the normal force coefficients of thinner profiles remain higher than the thicker ones.

TABLE 4 - REGRESSION NORMAL FORCE COEFFICIENTS OF VARIOUS PROFILES

| Rudder profile | Regression formula |
|---------------------------------|--|
| NACA 0012 | $C_{N(\Lambda=\infty)} = 6.1672\alpha_R$ |
| NACA 0015 | $C_{N(\Lambda=\infty)} = 6.1158\alpha_R$ |
| NACA 0018 | $C_{N(\Lambda=\infty)} = 5.9664\alpha_R$ |
| NACA 0021 | $C_{N(\Lambda=\infty)} = 5.6744\alpha_R$ |
| NACA 0024 | $C_{N(\Lambda=\infty)} = 5.3401\alpha_R$ |
| Empirical (No specific profile) | $C_{N(\Lambda=\infty)} = 6.13 \sin \alpha_R$ |

FIGURE 10 - COMPARISON OF NORMAL FORCE COEFFICIENTS OF VARIOUS PROFILES ($\Lambda = \infty$)

TURNING MANOEUVRES

Simulations were carried out using a simulation program written in Python with the ODE45 solver. Official turning circle tests were carried out with a starting speed of 15.5 knots, which is the default speed for KVLC2. The results are plotted in a bird's-eye view as can be seen in Figure 11 for the starboard turn and in Figure 12 for the portside turn. The macroscopic parameters that are derived from the simulations are summarised in Table 5.

It is interesting to observe that the trajectories of the NACA 0012, NACA 0015, and NACA 0018 are close to each other. With the estimated C_N of NACA 0021 and NACA 0024, the turning circle becomes larger. From NACA 0012 to NACA 0024, the turning advance and tactical

diameter increase about 5%. Due to the rotation direction of the propeller, the performance of portside manoeuvres and starboard manoeuvres are different.

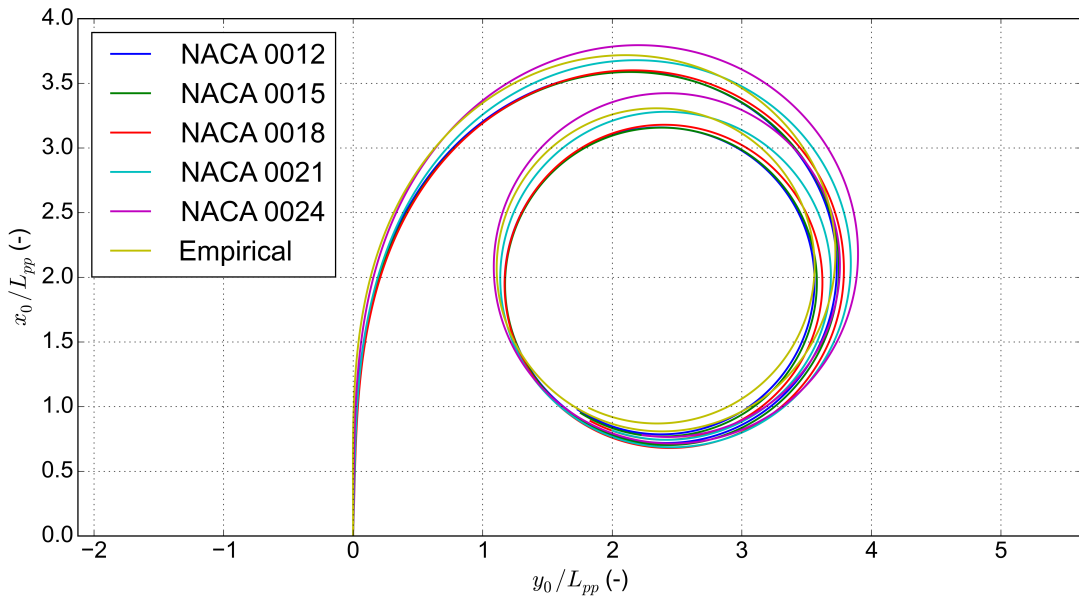


FIGURE 11 - SIMULATED SHIP TRAJECTORIES OF 35° STARBOARD TURN

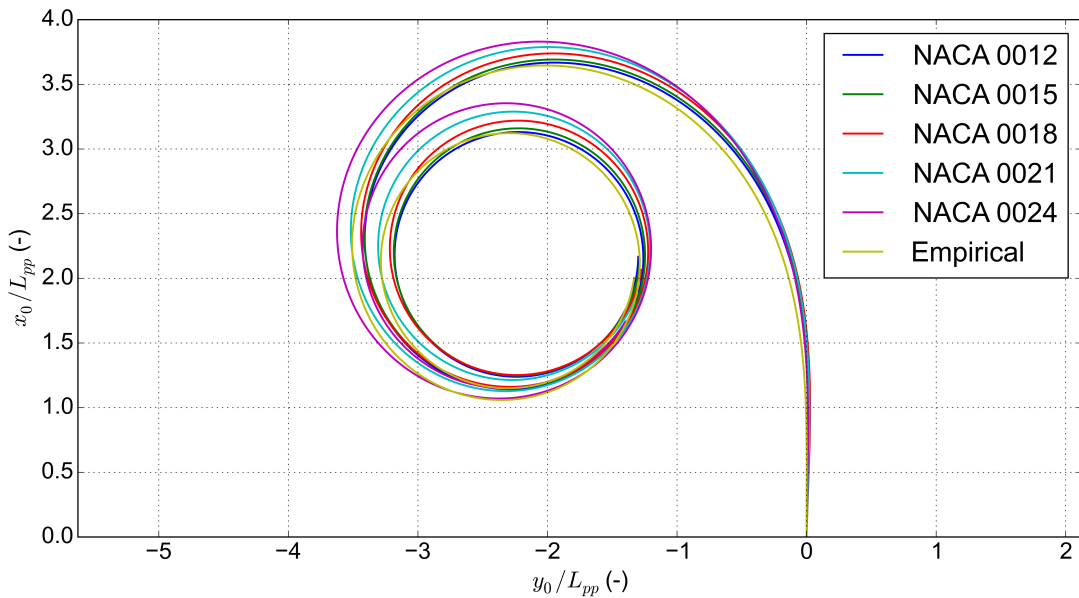


FIGURE 12 – SIMULATED SHIP TRAJECTORIES OF 35° PORTSIDE TURN

TABLE 5 - TURNING PARAMETERS OF SHIPS WITH VARIOUS RUDDER PROFILES

| Rudder Profile | 35° STARBOARD TURN | | 35° PORT TURN | |
|----------------|--------------------|-------------------|---------------|-------------------|
| | Advance | Tactical diameter | Advance | Tactical diameter |
| NACA 0012 | 3.527 | 3.668 | 3.601 | 3.342 |
| NACA 0015 | 3.521 | 3.685 | 3.626 | 3.344 |
| NACA 0018 | 3.534 | 3.722 | 3.672 | 3.371 |
| NACA 0021 | 3.614 | 3.775 | 3.723 | 3.450 |
| NACA 0024 | 3.730 | 3.832 | 3.765 | 3.557 |
| Empirical | 3.652 | 3.656 | 3.579 | 3.440 |

ZIGZAG MANOEUVRES

To quantify the course keeping abilities, zigzag manoeuvres were simulated. The results are plotted in time trace plots of rudder angle (δ) and heading angle (ψ) as can been seen in Figure 13 for 10°/10° zigzag tests and in Figure 14 for 20°/20° zigzag tests. From the time traces, the same trend can be observed as in the turning circle test, the ship reacts slower with NACA0021 and NACA0024, and faster with the thinner rudders. The resulting overshoot angles are summarised in Table 6. It is observed that especially for the 2nd overshoot angle in the 10°/10° zigzag manoeuvre, the overshoot angles are significantly affected by the choice of profile. The results of the 20/20° zigzag test and the results of the 35° turning circle manoeuvre are not so much influenced.

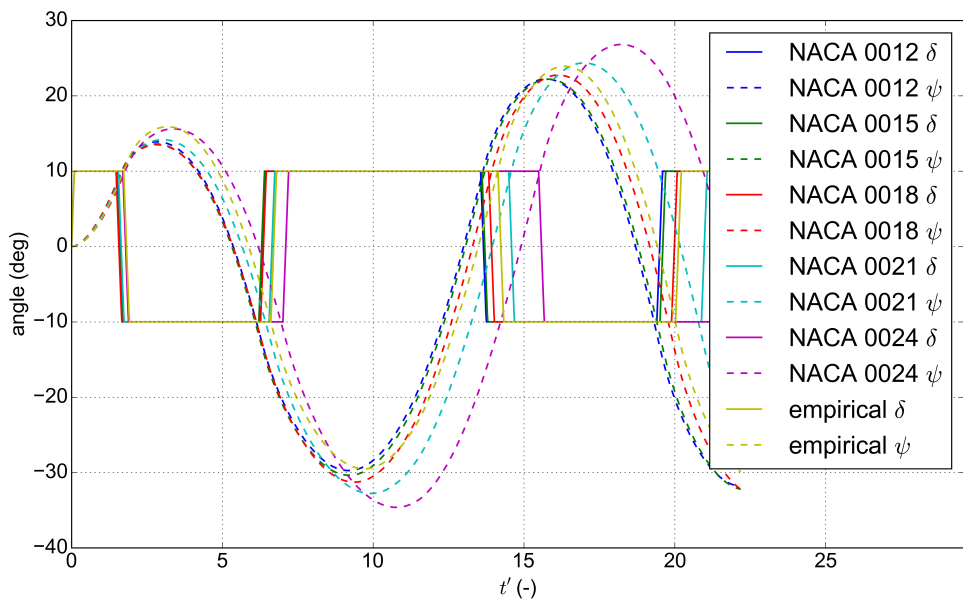


FIGURE 13 – SIMULATED TIME HISTORIES OF RUDDER ANGLE AND HEADING ANGLE IN 10°/10° ZIGZAG TESTS

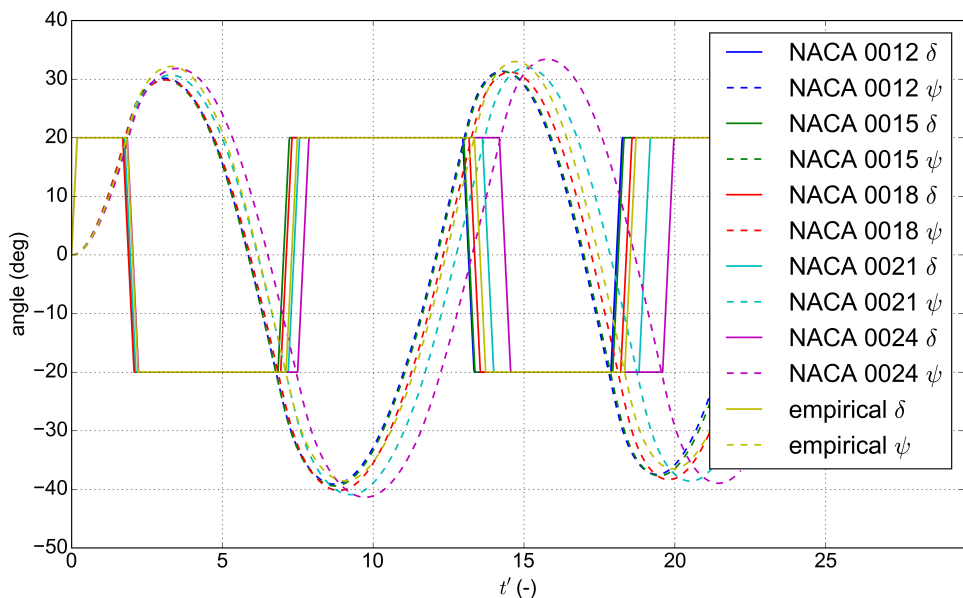


FIGURE 14 – SIMULATED TIME HISTORIES OF RUDDER ANGLE AND HEADING ANGLE IN 20°/20° ZIGZAG TESTS

TABLE 6 - SIMULATED OVERSHOOT ANGLES OF ZIGZAG TEST AS FUNCTION OF RUDDER PROFILE

| Rudder Profile | 10°/10° ZIGZAG | | 20°/20° ZIGZAG |
|----------------|----------------|---------------|----------------|
| | 1st OSA (deg) | 2nd OSA (deg) | 1st OSA (deg) |
| NACA 0012 | 5.280 | 18.353 | 11.523 |
| NACA 0015 | 5.321 | 18.748 | 11.643 |
| NACA 0018 | 5.372 | 19.411 | 11.721 |
| NACA 0021 | 5.733 | 21.240 | 12.233 |
| NACA 0024 | 6.498 | 23.744 | 12.693 |
| Empirical | 5.897 | 19.505 | 12.147 |

CONCLUSIONS

For a range of rudder profiles (rudder thicknesses), the effect of the rudder profile on the rudder normal force was estimated by performing 2D RANS simulations. These have resulted in estimations of the 3D rudder normal force. Regression formulas of rudder normal force coefficients were proposed for each tested NACA profile. It is clear that various rudder profiles have various hydrodynamic characteristics, which eventually affect the ship manoeuvrability. By using the results of the 3D rudder normal force in simulations, the effect of the rudder profile on the outcome of IMO manoeuvres can be quantified. This quantification led to the following insight:

- The largest effect was observed for the overshoot angles in the 10°/10° zigzag test.
- The results of the turning circle tests and of the 20°/20° zigzag test were less affected.

We realise that the above procedure is applied on just one ship, which is a marginally directional unstable vessel. It may be that the effect of these modifications on a directionally stable ship or a very directionally unstable ship are different. This may be a subject of further study.

REFERENCES

1. Fuji, H, & Tuda, T, (1961), "Experimental researches on rudder performance", Journal of the Society of Naval Architects of Japan, Vol. 109, pp. 31-42.
2. Kijima, K, Nakiri, Y, Katsuno, T, & Furukawa, Y, (1990), "On the manoeuvring performance of a ship with the parameter of loading condition", Journal of the Japan Society of Naval Architects and Ocean Engineers, Vol. 168, pp. 141-148.
3. Kim, Y. G, Kim, S. Y, Kim, H. T, Lee, S. W, & Yu, B. S, (2007), "Prediction of the maneuverability of a large container ship with twin propellers and twin rudders", Journal of Marine Science and Technology, Vol. 12, pp. 130-138.
4. Ladson, C, (1988), "Effects of independent variation of Mach and Reynolds numbers on the low-speed aerodynamic characteristics of the NACA 0012 airfoil section", Langley Research Center, Hampton, Virginia: National Aeronautics and Space Administration.
5. Langley Research Center, (2014), "Turbulence modeling resource", Retrieved from http://turbmodels.larc.nasa.gov/naca0012_val_sst.html
6. Molland, A. F, & Turnock, S. R, (2011), "Marine rudders and control surfaces: principles, data, design and applications (1st Edition)", Butterworth-Heinemann.

7. Quadvlieg, F. H. H. A, & Brouwer, J, (2011), "KVLCC2 benchmark data including uncertainty", The 4th International Conference on Computational Methods in Marine Engineering (MARINE 2011), Lisbon, Portugal, pp. 14..
8. Thieme, H, (1962), "Zur Formgebung von Schiffsrudern (in German)", Jahrbuch Schiffbautechnische Gesellschaft, pp. 381-426.
9. Yasukawa, H, & Yoshimura, Y, (2014), "Introduction of MMG standard method for ship maneuvering predictions", Journal of Marine Science and Technology, pp. 1-16.